

Proton therapy monitoring by Compton imaging: influence of the large energy spectrum of the prompt- γ radiation

Estelle Hilaire, David Sarrut, Françoise Peyrin
and Voichița Maxim

Université de Lyon, CREATIS, CNRS UMR5220, Inserm U1044, INSA-Lyon,
Université Lyon 1, France

E-mail: maxim@creatis.insa-lyon.fr

Received 8 June 2015, revised 24 February 2016

Accepted for publication 2 March 2016

Published 23 March 2016



CrossMark

Abstract

In proton therapy, the prompt- γ (PG) radiation produced by the interactions between protons and matter is related to the range of the beam in the patient. Tomographic Compton imaging is currently studied to establish a PG image and verify the treatment. However the quality of the reconstructed images depends on a number of factors such as the volume attenuation, the spatial and energy resolutions of the detectors, incomplete absorptions of high energy photons and noise from other particles reaching the camera. The impact of all these factors was not assessed in details. In this paper we investigate the influence of the PG energy spectrum on the reconstructed images. To this aim, we describe the process from the Monte Carlo simulation of the proton irradiation, through the Compton imaging of the PG distribution, up to the image reconstruction with a statistical MLEM method. We identify specific PG energy windows that are more relevant to detect discrepancies with the treatment plan. We find that for the simulated Compton device, the incomplete absorption of the photons with energy above about 2 MeV prevents the observation of the PG distributions at specific energies. It also leads to blurred images and smooths the distal slope of the 1D PG profiles obtained as projections on the central beam axis. We show that a selection of the events produced by γ photons having deposited almost all their energy in the camera allows to largely improve the images, a result that emphasizes the importance of the choice of the detector. However, this initial-energy-based selection is not accessible in practice. We then propose a method to estimate the range of the PG profile both for specific deposited-energy windows and for the full spectrum emission. The method relies on two parameters. We use a learning approach for their estimation and we show that it allows to detect few millimeter shifts of the PG profiles.

Keywords: proton therapy, monitoring, tomographic reconstruction, Compton camera, MLEM, Monte Carlo simulation

(Some figures may appear in colour only in the online journal)

1. Introduction

In proton therapy cancer treatments, interactions between the beam and the patient's body lead to nuclear reactions that produce secondary PG radiation. It was shown that some correlation exists between the emission point of those photons and the Bragg peak position (e.g. Kurosawa *et al* (2012), Min *et al* (2006), Stichelbaut and Jongen (2003) and Testa *et al* (2009)). Ongoing works aim to design imaging systems able to monitor the proton range by exploiting PG radiation. Among the proposed designs, we can mention SPECT systems such as knife-edge-slit, pinhole and parallel-slit collimator cameras (e.g. Bom *et al* (2012), Kim *et al* (2009), Lee *et al* (2012), Cambraia Lopes *et al* (2012), Perali *et al* (2014), Smeets *et al* (2012), Verburg and Seco (2014)), as well as Compton cameras (e.g. Frandes *et al* (2010), Kormoll *et al* (2011), Kurosawa *et al* (2012) and Richard *et al* (2012)). Both mechanically collimated SPECT systems and Compton cameras aim to determine the spatial distribution of the PG emission. Alternative approaches for the verification of the treatment are currently investigated. For instance, Verburg *et al* (2013) suggest to exploit the spatial variability of the gamma-ray spectrum and Golnik *et al* (2014) propose a method relying on timing measurements.

As mentioned by Polf *et al* (2009), the fall-off of the real PG profile is shifted from the Bragg peak because of the decrease in production of gamma rays for proton energies below of about 25 MeV. The profile reconstructed from the data shows additional offsets due to attenuation in the patient, acquisition factors and sequential errors introduced during data processing and image reconstruction steps.

During the treatment, secondary particles other than γ photons are produced. In the literature related to collimated cameras it is shown that those sources of noise may be partly avoided by adequate shielding of the detector (Min *et al* 2006), energy selection (Testa *et al* 2009, Smeets *et al* 2012) and time-of-flight selection (Verburg *et al* 2013, Pinto *et al* 2014). In a recent work, Ortega *et al* (2015) studied the influence of neutrons on the images obtained from Compton camera data. They also studied the noise induced by random coincidences that may occur when the detector becomes saturated. An other issue related to real-time quality control is the ability of the detection system to produce reliable outcome from a low number of data. In a simulation study, Lojacono *et al* (2013) evaluated from the reconstructed images the properties of the point spread function of a Compton camera as function of the number of detected events.

As already shown in Styczynski *et al* (2009) and more recently by Verburg *et al* (2013), the energy spectrum of the PG emission is spatially varying. At each given depth it depends on the residual energy of the beam. When a water phantom is irradiated with a proton beam, discrete gamma lines at 4.44, 5.2 and 6.13 MeV may be observed in the spectrum. Moreover, these lines are salient just before the end-of-range of the beam and disappear behind it. It is also known that the energy spectrum depends strongly on the irradiated tissue. Observation of the spectrum with a collimated camera may thus give important insight on the range of the beam (Polf *et al* 2009, Verburg *et al* 2013, Perali *et al* 2014) and on the chemical composition of the irradiated tissues (Moteabbed *et al* 2011, Polf *et al* 2009, 2013, Verburg and Seco 2014).

While the development of PG collimated cameras is advanced enough to allow tests in clinical conditions, they are still limited to provide 1D information. Next generation PG systems

should allow 2D or 3D imaging. The capability of Compton cameras to provide such images may be an important step forward for the monitoring of the treatment for beams going through heterogeneous tissues. In theory, the Compton camera efficiency is superior to Anger cameras, but it is also disadvantaged by the necessity to measure coincident events. Their capabilities struggle to convince and the performances of the available tomographic reconstruction algorithms is currently an important bottleneck. Some reconstruction algorithms were proposed in the literature, either based on analytic solutions (e.g. Maxim (2014), Smith (2005) and Tomitani and Hirasawa (2002)) or on iterative methods (e.g. Gillam *et al* (2011), Lojacono *et al* (2013), Mackin *et al* (2012) and Wilderman *et al* (1998)).

The main purpose of this paper is to investigate through simulations the capability of a proposed reconstruction algorithm to produce 3D maps of the PG distributions at given energies from the spectrum, to identify the limitations, and to extract from the images estimators of the fall-off position. To our knowledge, this is the first study of the 4D spatial and spectral PG distribution, with a Compton camera. As we focus on the analysis of the influence of the energy on the reconstructed images, number of noise sources were neglected and the number of emitted protons was set in the simulation to provide sufficient PG outcome for the reconstruction algorithm. The conclusions of our study were drawn for $4 \cdot 10^{11}$ emitted protons, although some illustrations concerning the total distribution are given for 10^9 primaries. As a comparison, the results from the measurements reported in Verburg *et al* (2013) for a collimated camera are means over 5 runs of 10^{10} primaries each. In Verburg and Seco (2014) a sub-millimeter precision on the proton range measurement was attained with $5 \cdot 10^8$ protons. When the number of primaries was lowered to 10^8 protons, the precision dropped to about 3 mm in water and about 4 mm in solid water. In Perali *et al* (2014) is shown that a slit camera allows to reach precision of 4 mm on range retrieval, with as few as about 10^8 protons. The PG profiles used in the study are samples drawn from a rescaled low-noise profile, by addition of Poisson noise. The reference low-noise profile was obtained by measuring the PG emission of a PMMA phantom irradiated with 10^{11} protons.

We simulated a two-stage Compton camera with limited footprint and design similar to the one described in Krimmer *et al* (2014). The camera is composed of seven layers of scatterer made in silicon and a 4 cm-thick absorber made of LYSO crystals. Because of incomplete absorptions, the information on the initial energy of the particles may be lost. An important issue from then is to determine the PG measured energy windows that provide relatively well reconstructed images and are thus best adapted to detect discrepancies with the treatment plan. PG profiles are extracted from the images and an estimator of the distal fall-off position is proposed and employed to characterize the ability of the simulated Compton camera to provide relevant information on the quality of the treatment by exploiting radiation in the selected energy window. Although our results are strongly related to the properties of the simulated camera, the proposed image reconstruction and range calculation methods could be applied to other designs.

2. Materials and methods

In this section, we present the different steps leading to the reconstruction of the Compton camera image of the PG distribution and to the estimation of the PG profile fall-off position. The proposed work-flow is summarized in figure 1. The irradiation of a water phantom with a proton pencil beam is simulated with the software GATE (Jan *et al* 2011, Sarrut *et al* 2014). A joint space-energy distribution $(v, \varepsilon) \in \mathbb{R}^3 \times \mathbb{R}_+^*$ $\mapsto \lambda(v, \varepsilon)$ is obtained and the marginal distribution $\lambda_{\text{tot}} = \sum_{\varepsilon} \lambda(\cdot, \varepsilon)$ is deduced. The simulation of the Compton imaging of

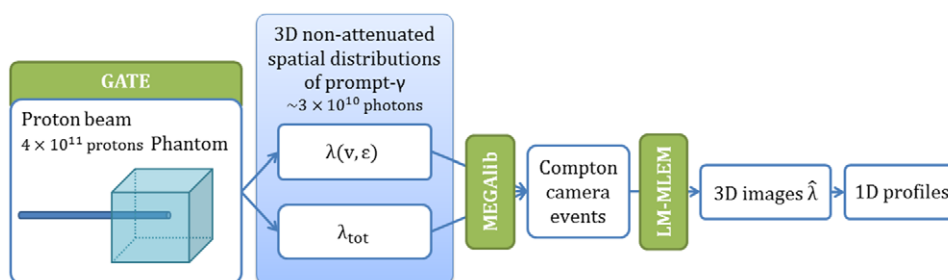


Figure 1. Simulation of the irradiation of a water phantom by a proton pencil beam with GATE. The distribution λ of the PG emission is extracted. The interaction of the PG photons in the Compton camera is simulated with MEGALib. The 3D distribution $\hat{\lambda}$ is reconstructed with a LM-MLEM algorithm and projected on the central beam axis to obtain a 1D profile.

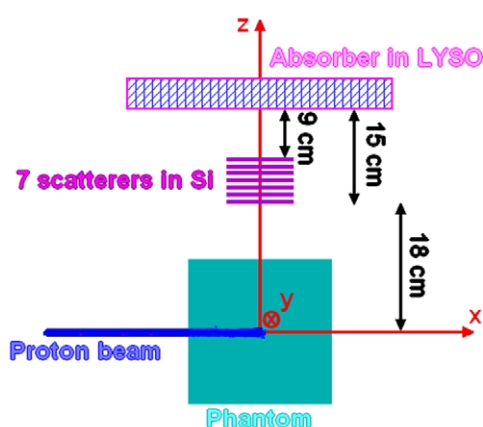


Figure 2. Architecture of the simulation.

the PG distributions is then realized with the software MEGALib (Zoglauer *et al* 2006). We introduce the method used to reconstruct the images from data recorded in the camera. Finally we present a method for the calculation of the depths from 1D profiles obtained from the reconstructed images.

2.1. Simulation process

2.1.1. Simulation of the prompt- γ emission. We simulated the irradiation of a water phantom of dimensions $(20\text{ cm})^3$ with a proton pencil beam of energy 120 MeV having 2D Gaussian profile with $(\sigma_y, \sigma_z) = (4, 2)$ mm (see figure 2). The pencil beam emits 4×10^{11} protons. Note that in clinical conditions, about 10^8 protons are emitted per spot, 10^{10} protons are generally used for the irradiation of the distant layer of the tumor and about 10^{11} protons are emitted per fraction of irradiation. Our set-up corresponds thus to the dose delivered to the entire treatment plan, concentrated in one single spot, which is probably above what could be achieved in clinic. However, taking into account the simulated efficiency of the modeled camera, which is of about 10^{-3} , the chosen intensity allows us to study the performances of the proposed reconstruction algorithm for different slices of the gamma energy spectrum.

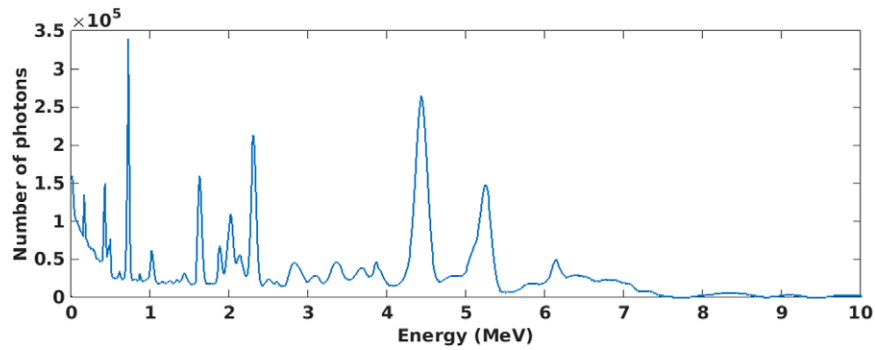


Figure 3. Energy spectrum $\sum_v \lambda(v, \cdot)$ of the PG radiation produced by a proton pencil beam of energy 120 MeV in water (bins of 10 keV).

The simulation of the irradiation was performed with GATE, a Geant4-based Monte-Carlo software. We used GATE version 7 with the QGSP_BIC_HP_EMY physics list, and Geant4 version 9.6.3. To limit the computation time, at this stage only 4×10^8 protons were simulated, the remaining 10^3 factor being applied to the PG distribution as mentioned below.

The non attenuated 4D joint energy-spatial frequency distribution λ of the PG emission was then recorded. The marginal distribution of the energy spectrum of the PG, cut at the interval (100 keV, 10 MeV), is shown in figure 3. Some dominant discrete γ lines may be observed, in particular those at 4.4 MeV and 5.2 MeV. They are produced by proton-induced reactions on ^{16}O at energies up to 50 MeV and were shown to characterize the end of the range of the beam (Verburg *et al* 2013). Note that all the secondary particles except PG were removed as soon as they were created.

Bins of $\Delta\varepsilon = 500$ keV were taken for the energy and the phantom was sampled into 100^3 voxels of 2 mm side. For each given energy bin having center ε_k and width $\Delta\varepsilon$, a three dimensional spatial distribution $\lambda(\cdot, \varepsilon_k)$ was obtained. It associates to each voxel v_j from the phantom volume the number $N_{k,j}$ of proton-induced photons emitted in the voxel v_j with an energy in the interval $[\varepsilon_k - \Delta\varepsilon/2, \varepsilon_k + \Delta\varepsilon/2)$. To decrease the variance induced by the limited statistics of the Monte Carlo simulation, the spatial distributions were smoothed with a 2D Gaussian filter having a FWHM of 2 pixels, for each slice parallel to the detector. The resulting distribution γ was then multiplied with 10^3 , leading to the targeted statistics that corresponds to 4×10^{11} emitted protons. Each voxel v_j of the volume was then considered as an isotropic mono-energetic source of photons. Note that this procedure leads to the loss of some physical information related to the PG particles, namely the exact emission positions and energies, and the direction of the particles. In turn, it allows to lower the computational cost of the simulation and to reduce the influence of statistical fluctuations. Fast simulation of PG emission is a topic of high importance for proton-therapy monitoring. A method based on track length estimator was recently proposed in Kanawati *et al* (2015).

2.1.2. Simulation of the Compton camera acquisition. The simulated camera consists of a scatterer made of seven silicon layers of dimensions $9.6 \times 9.6 \times 0.2$ cm³ with 1 cm gap between two successive layers, placed at 9 cm distance from an absorber made of LYSO measuring $37 \times 37 \times 4.2$ cm³. Each silicon scatterer contains 2×128 strips with energy resolution of 2.35 keV FWHM. The LYSO crystals of the segmented absorber measure $0.5 \times 0.5 \times 4$ cm³ each and have an energy resolution depending upon a Gaussian distribution on the energy of

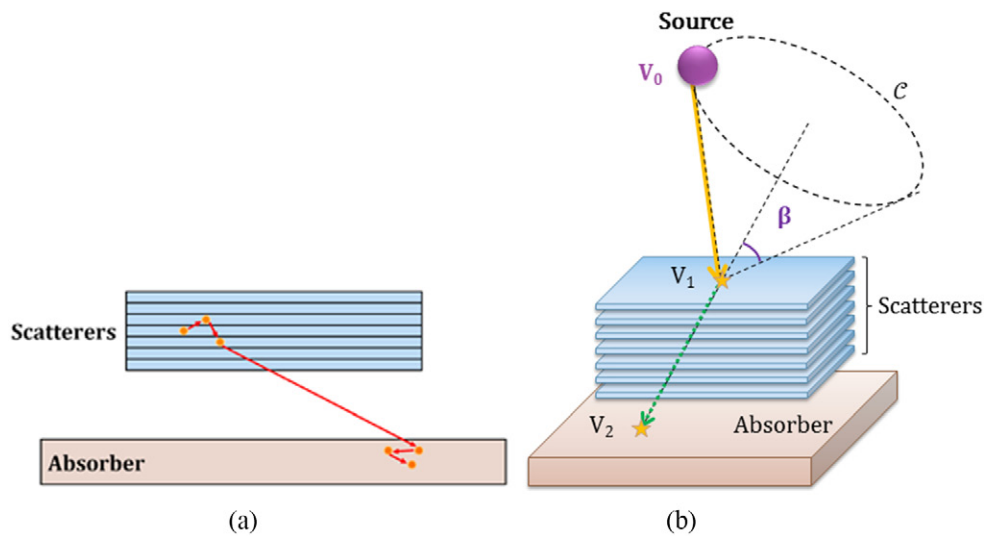


Figure 4. (a) A γ photon undergoes Compton scatterings in a first detector called scatterer, that might be composed of several layers, and is finally absorbed in a second detector called absorber. The order in the sequence of interactions cannot be established but only estimated. (b) From position and energy measures, the point that generated the photon is located on the surface of the cone. (a) Sequence of Compton interactions. (b) Compton camera principle.

the incoming photon. The standard deviation σ of the Gaussian varies from 3.5% to 1.2% in the range of 0.1 MeV to 10 MeV. The assumed energy resolution is too optimistic in view of new data (Roemer *et al* 2015), but has no major impact on the results presented here. The camera and its positioning with respect to the phantom are shown in figure 2. The position of a hit in the absorber is calculated with a barycentric rule and the z coordinate is set as the middle of a crystal (the depth of interaction is supposed unknown).

The Compton camera acquisition of the γ photons was simulated with the software Cosima (Zoglauer *et al* 2009), part of MEGALib version 2.28. Built on Geant4 too, this software was designed for Compton camera simulated and real experiments.

The individual recording of the photons avoids random coincidences. An event is triggered when at least one interaction is detected in each detector of the camera. Spatial and energy resolutions of the detectors and Doppler broadening are accounted for. The order of the hits of a given photon is supposed unknown and the most likely path is calculated from interaction positions and deposited energies with the software Revan, also part of the MEGALib library.

The Compton camera detects a photon in two steps. The photon, having initial energy E_0 , is scattered in a first detector (scatterer) at some position V_1 and deposits an energy denoted E_1 . The scattered photon may further interact in the first detector and, ideally, is finally absorbed in a second detector (absorber) by photoelectric effect (see figure 4). The energy deposited by the photon after the first Compton scattering will be denoted hereafter E_2 . Ideally, the remaining energy $E_0 - E_1$ is entirely deposited in the camera and we should have $E_0 = E_1 + E_2$. If this is the case, the conservation law of energy allows to recover the scattering angle of the photon (Compton 1923) through the equation:

$$\cos \beta = 1 - \frac{m_e c^2 E_1}{E_2 (E_1 + E_2)}, \quad \text{with } m_e c^2 = 511 \text{ keV.} \quad (1)$$

Generally a part of the initial energy is deposited in non sensitive material or is taken away by the photon or its derivatives escaping from the device. Thus, the measured total energy $E_{\text{tot}} = E_1 + E_2$ does not always match the initial energy E_0 , leading to an overestimation of the Compton angle.

In case of multiple interactions in the camera (the most probable case in case of high energies), the Revan software decides which of the interaction locations is taken as the first and second ones defining the cone axis. The energy associated to the hit identified to be the first is considered from then as E_1 and E_2 comprises the sum of all energies deposited in the other hits. The calculated positions of the first and second hit, denoted V_1 and V_2 , and the energies E_1 and E_2 define an event $e = (V_1, E_1, V_2, E_2)$. The incoming path of the initial ray is then supposed to lie on the surface of the cone defined by the apex V_1 , the half-opening angle β (i.e. the scattering angle of the photon) and the axis direction $\overrightarrow{V_2V_1}$ (see figure 4(b)).

2.2. Reconstruction method

Let $(e_i)_{i=1, \dots, N_e}$ be the list of recorded events and $(\lambda_j)_{j=1, \dots, N_v}$ be the discretized 3D image of the source, with N_v the total number of voxels. The 3D image is reconstructed using the LM-MLEM algorithm (Shepp and Vardi 1982, Wilderman *et al* 1998). From an initial estimate $\lambda^{(0)}$, the algorithm calculates successive approximations $\lambda^{(\ell)}$ of $\hat{\lambda}$, the maximum likelihood estimator of the image. The sequence $\lambda^{(\ell)}$ is supposed to converge towards the vector λ representing the mean emission intensities in the voxels of the volume. The iterations are based on the equation:

$$\lambda_j^{(\ell+1)} = \frac{\lambda_j^{(\ell)}}{s_j} \sum_{i=1}^{N_e} t_{ij} \frac{1}{p_i^{(\ell)}}, \text{ with } p_i^{(\ell)} = \sum_{k=1}^{N_v} t_{ik} \lambda_k^{(\ell)}, \tag{2}$$

where t_{ij} is the probability for a photon emitted by the voxel v_j to be detected as event e_i and s_j is the probability for a photon emitted by the voxel v_j to be detected. The matrix $T = (t_{ij})_{i=1, \dots, N_e, j=1, \dots, N_v}$, generally called the system matrix, and the sensitivity $S = (s_j)_{j=1, \dots, N_v}$ are the key parameters of the algorithm.

2.2.1. Calculation of the system matrix. The system matrix T accounts for the specific conical shape of the set of source points that could produce an event and for the known energy uncertainties of the detector through a spatial kernel h_i . For a given event $e_i = (V_1, E_1, V_2, E_2)$ let us denote β_i the estimated Compton angle. We define h_i as a Gaussian of mean β_i and standard deviation σ_{β_i} calculated, as suggested by Ordonez *et al* (1997), from the deposited energies and the resolution of the detectors as:

$$\sigma_{\beta_i} = \frac{m_e c^2}{\sin \beta_i} \sqrt{\left(\frac{1}{E_1^2} - \frac{1}{E_{\text{tot}}^2}\right)^2 dE_1^2 + \frac{dE_2^2}{E_{\text{tot}}^4}}. \tag{3}$$

Let M be a point from the volume to reconstruct. For δ_M the angular distance between $\overrightarrow{V_2V_1}$ and $\overrightarrow{V_1M}$, the expression of the spatial kernel is then:

$$h_i(M) = \frac{1}{\sqrt{2\pi} \sigma_{\beta_i}} \exp\left(-\frac{1}{2} \left(\frac{\delta_M - \beta_i}{\sigma_{\beta_i}}\right)^2\right). \tag{4}$$

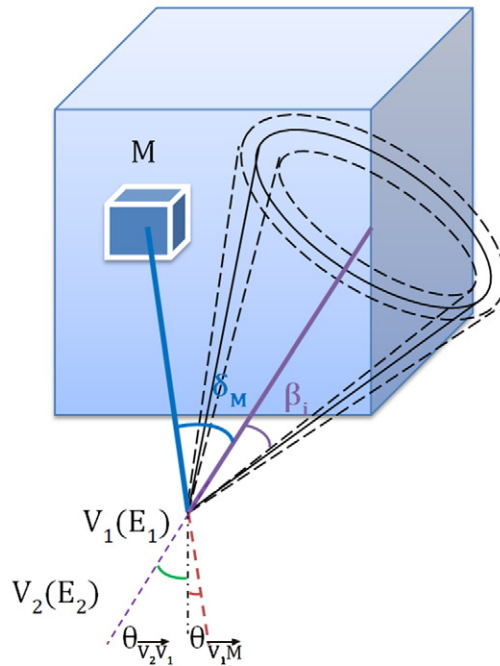


Figure 5. Parameters for the calculation of the probabilities t_{ij} .

For a given vector \vec{w} , we denote $\theta_{\vec{w}}$ the angle between \vec{w} and the normal to the camera. Figure 5 shows the parameters entering in the definition of the system matrix. According to Maxim *et al* (2016), we model the elements of the matrix T as:

$$t_{ij} = \frac{|\cos(\theta_{\vec{v}_2\vec{v}_1})|}{\|\vec{v}_2\vec{v}_1\|} \int_{M \in v_j} K(\delta_M, E_{\text{tot}}) \frac{|\cos(\theta_{\vec{v}_1\vec{M}})|}{\|\vec{v}_1\vec{M}\|^2} h_i(M) dv, \tag{5}$$

where $K(\delta_M, E_{\text{tot}})$ is the Compton scattering cross section with parameters calculated from the data. The spatial kernel h_i allows to account for measurement uncertainties by considering that every point of the image may produce the given event, with a probability depending on its angular distance to the surface of the associated Compton cone.

For the numerical evaluation of (5), we denote O_j the center of the voxel v_j and we propose to use the approximation:

$$t_{ij} = K(\delta_{O_j}, E_{\text{tot}}) \frac{|\cos(\theta_{\vec{v}_2\vec{v}_1})|}{\|\vec{v}_2\vec{v}_1\|} \frac{|\cos(\theta_{\vec{v}_1\vec{O}_j})|}{\|\vec{v}_1\vec{O}_j\|^2} h_i(O_j), \text{ if } |\delta_{O_j} - \beta_i| \leq 3\sigma_{\beta_i}, \tag{6}$$

and $t_{ij} = 0$ otherwise. Proportionality to the volume of the voxel was ignored in (6).

2.2.2. Calculation of the sensitivity. The sensitivity $S = (s_j)_{j=1, \dots, N_v}$, that allows in (2) to compensate for the loss of photons emitted in distant voxels, can be assessed either by Monte Carlo simulation or approximated analytically as in Wilderman *et al* (2001). In the reconstructions performed in this work, the calculation method did not have a significant influence on the results. The analytical method was hereafter chosen for its satisfactory performances at negligible computational cost.

The analytical computation consists in considering some simplifications in the detector's geometry. Assuming that the absorber is wide compared to the scatterer and placed close to it, that the Compton cross sections $K(\beta, E_{\text{tot}})$ have similar influence for all voxels and that the size of a voxel is small, the variations in s_j are essentially due to variations of the solid angle subtended by the scatterer volume at the centre O_j of the voxel. Assuming that the side of the scatterer is small compared to the distance from the source to the detector, we put:

$$s_j \propto \frac{|\cos(\theta_{\vec{QO}_j})|}{\|QO_j\|^2}, \quad (7)$$

where Q is the center of the scatterer block.

2.3. Calculation of the depth of the distal fall-off of the prompt- γ profile

Compared to the dose fall-off which corresponds to a limit on the irradiated region, the PG profile fall-off has less meaning for the treatment. Its main role is to provide a quantitative tool for the measure of range shifts. In the literature, its estimation vary as function of the detection system.

Let us call f the 1D profile obtained by projecting the 3D PG distribution λ on the proton central beam axis. The fall-off of the simulated PG profile was taken as it is usually done for the Bragg peak at 80% of the maximum value M , i.e. $d = f^{-1}(0.8M)$. For the reconstructed profiles, the abscissa of the point where the profile drops under 80% of the maximum value is not always suitable and presents some variability. Depending on the shape of the curve, a specific percentage or a mean over a range of percentages may be more convenient.

For high-variability curves, we suggest to calculate the fall-off as the mean over a range of percentages $[p_{\min}, p_{\max}]$ according to:

$$\hat{d}_{p_{\min}, p_{\max}} = \frac{1}{(p_{\max} - p_{\min})M} \int_{p_{\min}M}^{p_{\max}M} f^{-1}(y)dy \quad (8)$$

An example is illustrated in figure 6. The range $[p_{\min}M, p_{\max}M]$ is displayed in blue and the mean value $\hat{d}_{p_{\min}, p_{\max}}$ is represented by the green line. It may be shown that the two areas to the left and right of the mean, highlighted in blue, are equal.

For profiles showing low variability, one may take $p_{\min} = p_{\max}$, leading to the estimated fall-off position $\hat{d}_{p_{\min}, p_{\max}} = f^{-1}(p_{\min}M)$.

Some other methods have been proposed in the literature. In Ortega *et al* (2015), the value of M is the height of the deepest peak and $\hat{d} = f^{-1}(0.8M)$ or $\hat{d} = f^{-1}(0.5M)$. For profiles presenting important variability, a prior fit of the data with some smooth function is recommended (Smeets *et al* 2012, Gueth *et al* 2013, Janssen *et al* 2014).

Obviously, it exists an infinity of couples of parameters (p_{\min}, p_{\max}) leading to $\hat{d}_{p_{\min}, p_{\max}} = d$. An important issue from then is the choice of the parameters and it seems reasonable to learn the values from some previous experience. Two examples will be given in section 3.4.

2.4. Calculation of the range shift

One of the challenges for a proton therapy monitoring system is the range shifts detection. By analogy with the beam range, we define the PG deduced proton range as the distance from the phantom entry to the fall-off position of the PG profile.

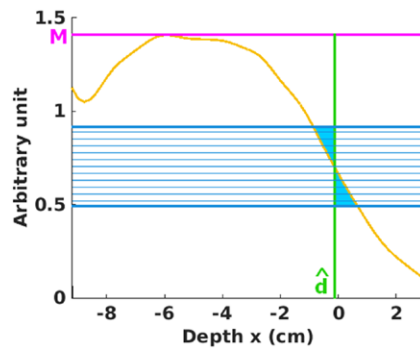


Figure 6. Depth calculation.

A shift of 5 mm is produced by increasing the beam energy from 120 MeV to 123 MeV. The same result is obtained when the energy increases from 123 MeV to 126 MeV. At 120 MeV, the simulated Bragg peak is located at $x = 6$ mm, which corresponds to a range of the beam in the phantom of 106 mm. As expected, the PG deduced proton range is shorter and measures 100 mm.

We define the estimated range shift induced by the increase of the energy of the beam as the difference between the corresponding estimated fall-off positions.

3. Results

3.1. Prompt- γ distribution as function of the energy

Figure 7 shows 2D slices from the 3D distributions $\lambda(\cdot, \varepsilon_k)$ of the PG rays produced in the phantom, for the energy bins described in section 2.1.1. It should be noticed that the color scale differs from one slice to another.

It may be seen that the energies up to 1.5 MeV are more represented at the beginning of the path of the beam. For some other energies, the distribution presents a peak close to the end-of-range. This is the case for instance for the windows [4–4.5] MeV and [5–5.5] MeV which include two of the remarkable gamma lines mentioned by, e.g. Verburg *et al* (2013).

3.2. Influence of the prompt- γ energy on the reconstructed images

The distributions simulated as described in section 2.1.1 and plotted in figure 7 were then used to generate Compton camera data. For each distribution, a volume of $20 \times 8 \times 2.5$ cm³ divided in $100 \times 41 \times 13$ voxels centered on the axis of the beam was reconstructed with the iterative LM-MLEM algorithm described in section 2.2. Central horizontal slices from the results at iteration 15 are shown in figure 8. Given the considered geometry, the acquired Compton projections are truncated. Despite correction with the sensitivity factor in (2), the reconstructed images are still not quantitative. Therefore, the color scales are not displayed in figures 8 and 9. Less studied for Compton tomography, the topic of image reconstruction from incomplete projections is better understood in classical tomography and some analytical conditions leading to uniqueness of the solution of the region of interest imaging problem were established. In Zhang and Zeng (2007), the properties of the MLEM algorithm are investigated and compared to analytical solutions. The MLEM algorithm is shown to give in practice better results than analytical methods when the uniqueness conditions are not verified.

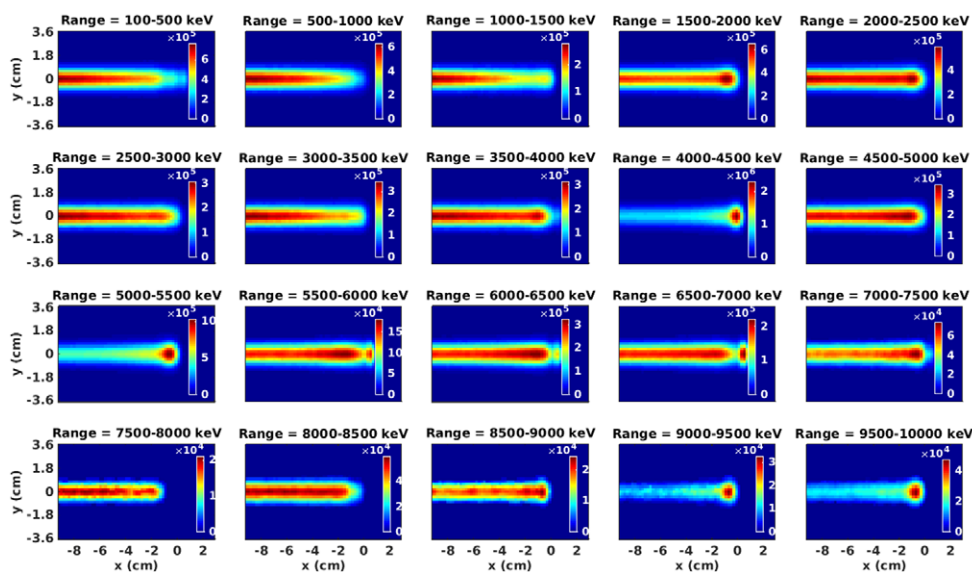


Figure 7. 2D slices from the 3D distributions $\lambda(\cdot, \varepsilon_k)$ of PG rays produced by the irradiation of a water phantom with a proton pencil beam of energy 120 MeV. Energy windows between 100 keV and 10 MeV sampled with a 500 keV step. Central slices at $z = 0$ cm of width 2 mm.

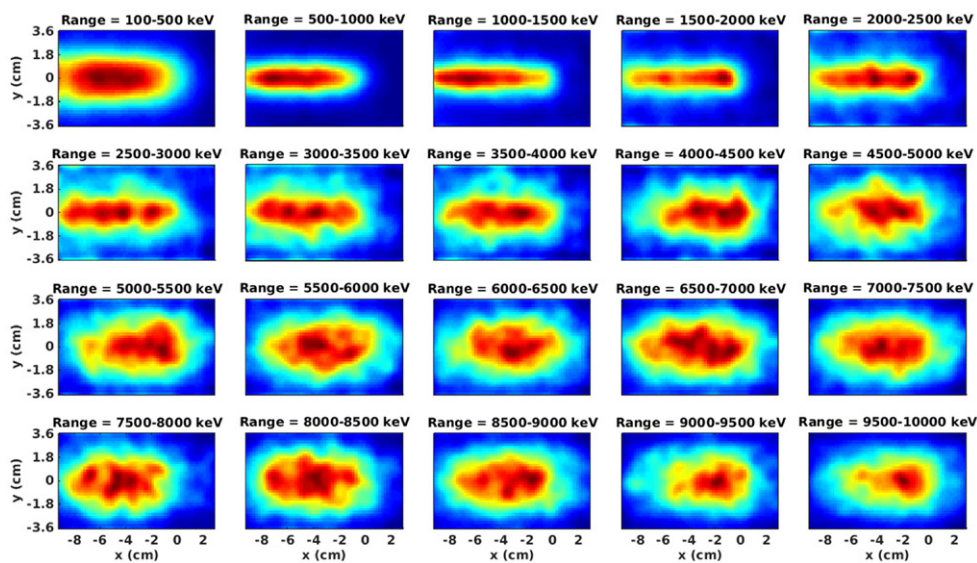


Figure 8. Reconstructed images of the PG distribution $\hat{\lambda}(\cdot, \varepsilon_k)$. See figure 7 for the reference distributions.

It may be observed that the accuracy of the reconstructed images decreases as the energy increases. An explanation is that at relatively high energies, the photons undergo numerous interactions in the camera and also are more likely to be incompletely absorbed (see figure 10). The errors on the estimated Compton angle and on the reconstructed sequence of

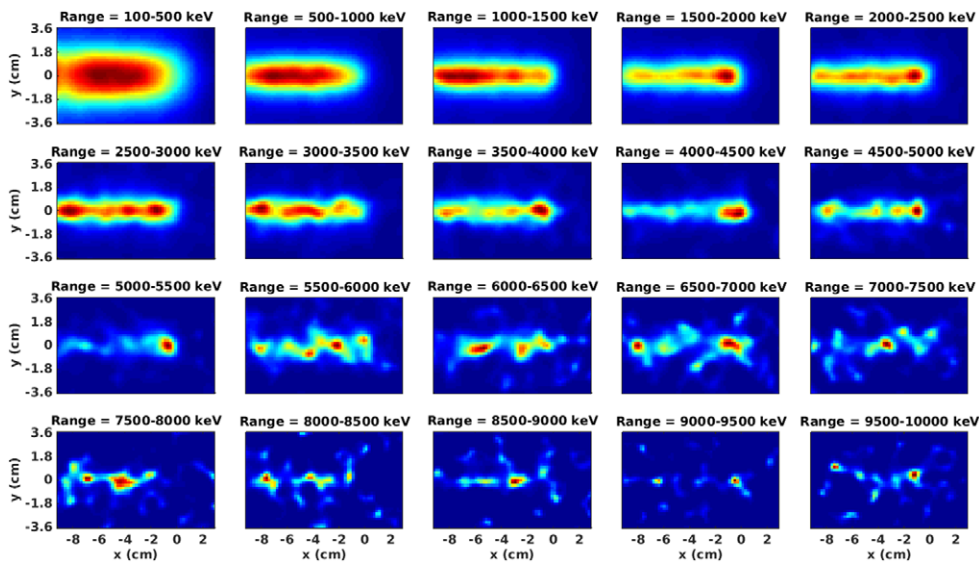


Figure 9. Reconstructed images of the PG distribution $\hat{\lambda}(\cdot, \varepsilon_k)$ after selection of the events having deposited a total energy E_{tot} verifying $|E_{\text{tot}} - E_0| \leq 250$ keV. See figures 7 and 8 for a comparison.

hits lead to the blurring of the reconstructed distribution. Although the range of the beam is still roughly identifiable, the sharpness of the PG distribution is lost at the higher energies.

Some improvement may be obtained by imposing an energy selection to the detected events, i.e. selecting events whose total deposited energy belongs to a given window. Figure 9 shows slices reconstructed from only events for which the absolute error on the total energy $|E_{\text{tot}} - E_0|$ is below $\Delta\varepsilon/2 = 250$ keV.

It may be seen from figures 8 and 9 that in the window $[0.1, 2]$ MeV, the improvement produced by the energy selection is incremental. The differences are more striking above 2.5 MeV and the energy selection largely benefits to the peaked distributions from the bins $[4, 4.5]$ MeV and $[5, 5.5]$ MeV.

The evolution of the quality of the images with the energy of the γ photons may be more easily observed on the profiles plotted in figure 11. The profiles are calculated as projections from the central slice on 1 cm around the line $y = 0$ cm. This lateral integration does not cover the full 2D distribution but the chosen interval includes the relevant information around the axis of the beam and partly rule out the blur. The influence of the energy selection (dashed blue lines) is obvious above about 2 MeV. Up to 6 MeV the profiles reconstructed after energy selection are very close to the PG profile, especially near to the fall-off where they are almost confounded. Without energy selection, the reconstructed profiles are close to the simulated profile only up to about 2 MeV.

For energies above 6 MeV, the number of available events drops under $1.5 \cdot 10^3$ and the results are hardly exploitable whatever the energy selection parameter. Indeed, the modeled Compton camera does not correctly detect high energy photons. As shown in figure 12(a), the number of events selected as valid by the reconstruction algorithm decreases with the energy. Also, at the higher energies, the number of hits per incident photon increases. E.g. at 4.5 MeV, the photons interact with energy deposits above 20 keV, in average 2.3 times in the absorber and 5.8 times in the scatterer. In addition, when looking at figure 12(b),

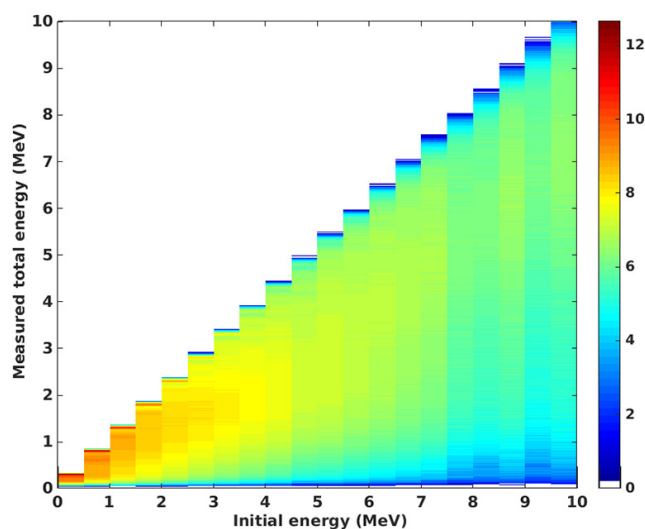


Figure 10. Distribution of the total measured energy as a function of the initial energy (logarithmic scale). The distribution of the initial energy is the one plotted in figure 3.

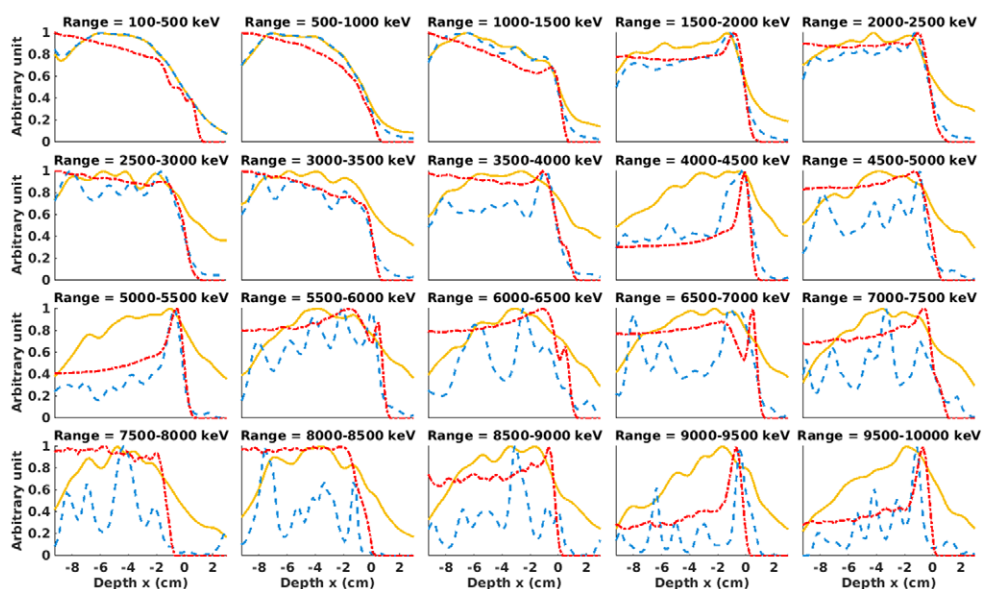


Figure 11. Overlay of three PG profiles: reference (dotted red line), reconstruction from events with total energy E_{tot} verifying $|E_{\text{tot}} - E_0| \leq 250$ keV (dashed blue line) and reconstruction from all the events (solid yellow line), for energy windows between 100 keV and 10 MeV with a 500 keV step. Projections calculated from the central slice on 1 cm around the line $y = 0$ cm.

it appears that the proportion of completely absorbed events (with a tolerance of ± 250 keV) among all the valid events decreases quickly with the energy. This means that more the energy increases, greater the number of noisy events becomes. The reconstruction of a photon path in the camera becomes complex, the Compton angle is overestimated and the

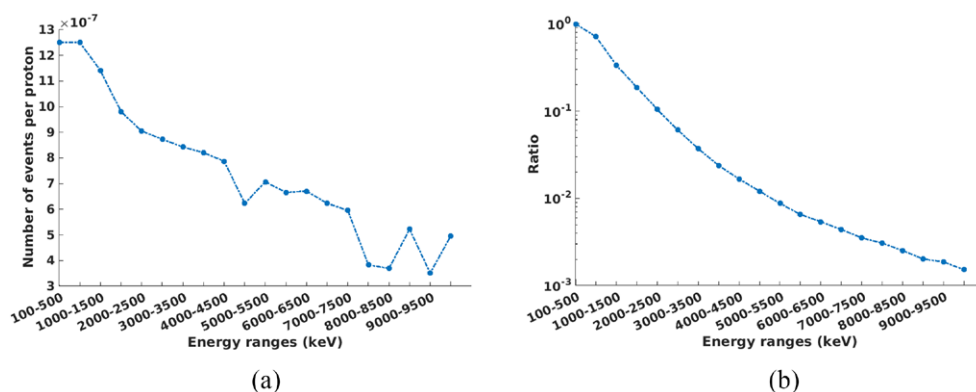


Figure 12. (a) Number of events selected as valid by the reconstruction algorithm without energy selection, per emitted proton. (b) Proportion of events selected as completely absorbed with $|E_{\text{tot}} - E_0| \leq 250$ keV, among all valid events.

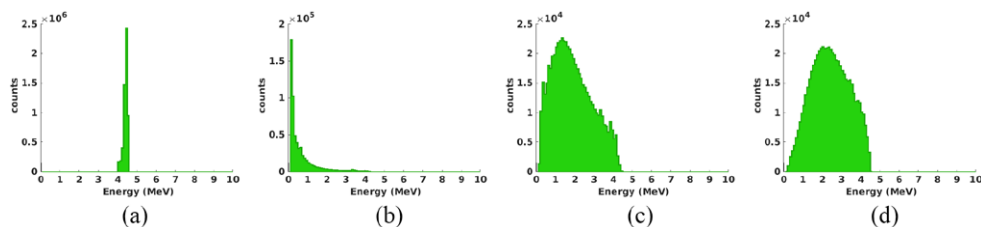


Figure 13. Energy spectra for events detected with initial energy between 4 MeV and 4.5 MeV. Counts obtained for 4×10^{11} emitted protons. (a) Initial energy spectrum. (b) Distribution of energies transferred to electrons (first hit). (c) Energy spectrum of the scattered photons. (d) Energy spectrum of coincident events.

images are less accurate. Random coincidences and detector load were not accounted for in the study. It may be mentioned that the observed mean number of hits per emitted proton was $4.65 \cdot 10^{-5}$ for the scatterer block and $2.33 \cdot 10^{-5}$ for the entire segmented absorber block.

3.3. Influence of the measured total energy selection on the reconstructed images

The limited capability of the camera to provide the initial energy of the incoming photons makes impossible to observe the spatial distribution at some given initial energy. As an example, in figures 13 and 14, we observe the spectra of initial and measured energies from events with energy in the windows [4, 4.5] MeV and [0.1, 10] MeV. The distribution from figure 14(a) is the same as in figure 3 and the figure 13(d) is the plot of a column from figure 3. In each figure, panel (a) represents the initial energy spectrum. Panel (b) display the distribution of the energy transferred to the electron at the first hit. Panel (c) shows the distribution of E_2 , the energy deposited in the camera by the scattered photon. The last panel (d) represents the measured sum energy spectrum of coincident events in the camera.

The images shown on the upper row of figure 15 represent slices of the simulated PG spatial distribution for some selected initial energy windows. The windows are R_{tot} , which contains all the events, $R_1 = [0.5, 2.5]$ MeV, $R_2 = [4, 4.7]$ MeV and $R_3 = [4.7, 5.5]$ MeV.

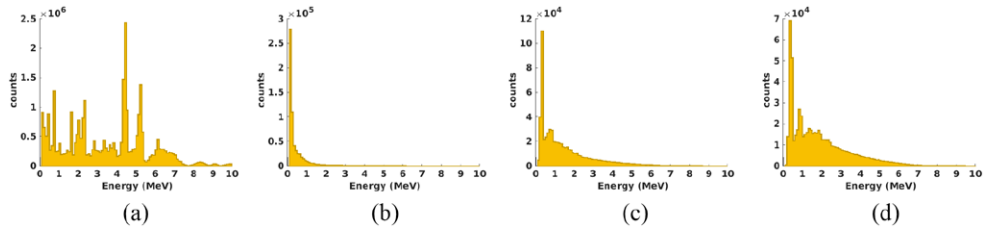


Figure 14. Energy spectra for events detected with initial energy between 100 keV and 10 MeV. Counts obtained for 4×10^{11} emitted protons. (a) Initial energy spectrum. (b) Distribution of energies transferred to electrons (first hit). (c) Energy spectrum of the scattered photons. (d) Energy spectrum of coincident events.

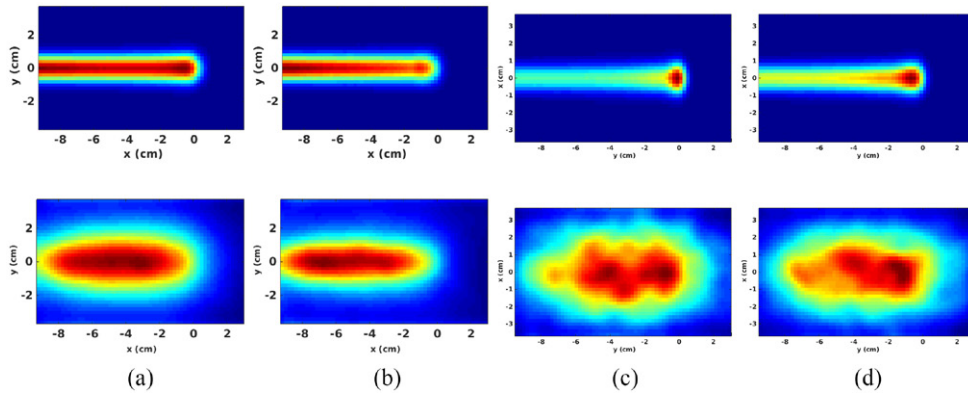


Figure 15. PG distributions for different energy windows. Upper line: simulated reference distributions. Bottom line: reconstructed distributions. (a) All events. (b) Events with total energy in $R_1 = [0.5, 2.5]$ MeV. (c) Events with total energy in $R_2 = [4, 4.7]$ MeV. (d) Events with total energy in $R_3 = [4.7, 5.5]$ MeV.

These reference distributions obtained from simulations serve for comparison for the reconstructed images shown on the bottom row. The reconstructed images are produced by selecting from the data only the photons having deposited in the camera an energy E_{tot} belonging to the specified range. The slices are obtained from volumes whose dimensions and number of voxels are the same as in section 3.2. On the first column, the distributions λ_{tot} and $\hat{\lambda}_{\text{tot}}$ include PG of all energies and the reconstructed image is calculated from 4.85×10^6 events in 15 iterations. The number of events available for windows R_1 , R_2 and R_3 was respectively 2×10^6 , 1.58×10^5 and 1.1×10^5 events. The first energy window R_1 was chosen as it contains energies well suited for the modeled camera. Moreover, the resulting image and profile show low variance. The two other windows were chosen as corresponding to salient peaks in the energy spectrum of the PG emission, and to spatial distributions relatively well reproduced in figures 8 and 11.

3.4. Detection of shifts

The aim of this section is to evaluate the ability of the Compton camera to identify range shifts. As explained in sections 2.3 and 2.4, we first need to calculate fall-off positions, that were defined as functions of two parameters p_{min} and p_{max} .

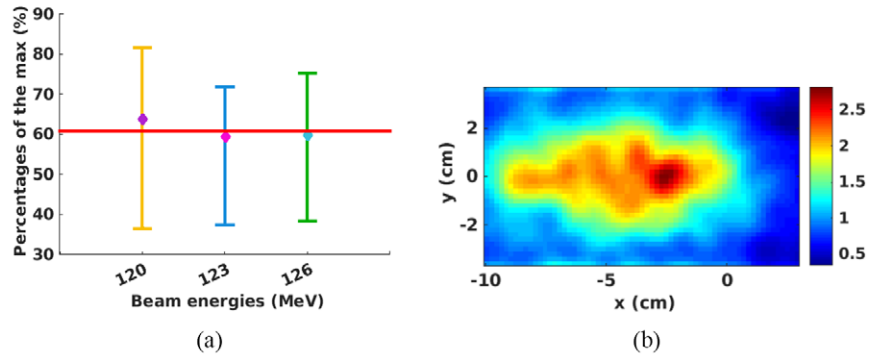


Figure 16. (a) Percentages of the maximum value of the profile, corresponding to the simulated PG position, calculated over 100 samples (10^4 events each and 15 iterations) for each of the 3 beam energies. Diamonds represent median values and the vertical lines connect the minimum and maximum values. (b) Exemple of image reconstructed from 10^4 events and 15 iterations, without energy selection. Figure 15(a) shows the image of the same distribution reconstructed from 4.85×10^6 events.

3.4.1. Variability of the best percentage value. For each beam energy, we reconstructed 100 profiles from 10^4 events each, without any energy selection. For each profile f_k obtained from the samples, we evaluated the p_k percentage of the maximum M_k of the curve, corresponding to the simulated fall-off d , as:

$$p_k = \frac{f_k(d)}{M_k} \times 100\%. \quad (9)$$

Then, we calculate the maximum, the minimum and the median of the values p_k for $k = 1, \dots, 100$ and the 3 beam energies. The results are plotted in figure 16(a). The median values over the samples are pictured by the diamonds on the line segments. The extremities of the line segments correspond to the extreme values. The central red line $y = 60.81\%$ represents the median over all the values whatever the beam energy.

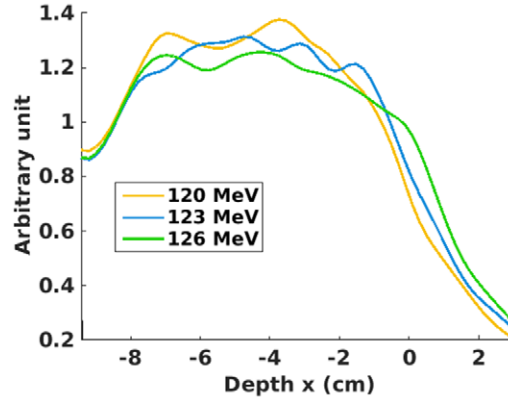
It may be seen from figure 16(a) that the median values are close one to another for the three considered energies. This suggest that the median percentage calculated for one given energy may be extrapolated for other energies.

Note that for the efficiency of the considered camera, 10^4 detected photons correspond to about 10^9 emitted protons, i.e. to 10 of the stronger spots. The mean values over the 100 samples of the errors $|\hat{d}_{p_{\min}, p_{\max}} - d|$ with $p_{\min} = p_{\max} = 0.61$, are for the three considered energies of 2.2, 2.9 and 3.3 mm. The standard deviations are 3.1, 5 and 5.8 mm. In clinical conditions, we may thus expect an average error of 3 mm on the estimated fall-off, but the results present a large variance.

3.4.2. Estimation of the shift for the statistically learned best percentage. The statistical study from the previous section 3.4.1 gives a median best percentage value. We applied the method described in section 2.3 to estimate the PG deduced proton range for the total reconstructed profiles, i.e. profiles reconstructed without any energy selection, for each of the three beam energies. The profiles are shown in figure 17. We choose $p_{\max} = p_{\min} = 60.81\%$, the median over the values p_k calculated for the 100 profiles and three energies. We can see from table 1 the PG deduced proton range is very well estimated with a sub-millimetric error.

Table 1. Error on the estimated PG deduced proton range, in millimeters.

Beam energy	120 MeV	123 MeV	126 MeV
PG deduced proton range (mm)	100	105	110
Error (mm)	0.2	0.5	0.9

**Figure 17.** Overlay of profiles reconstructed from all events.

However, we can apply this method only to profiles from a set-up identical to the one for which the learning was done. The best percentage calculated for profiles reconstructed from all data cannot be extrapolated to profiles calculated following energy selection.

3.4.3. A posteriori error. For the three energies of the proton beam, overlays of reference and reconstructed profiles are shown in figure 18. The slope of the reconstructed profiles near the Bragg peak is less sharp than for the profiles obtained by energy selection and shown in figure 11. For all beam energies, the total reconstructed profile is closer to the R_1 profile and likewise, the R_2 and R_3 curves are very similar.

Figure 18 shows that the 80% criterion used to calculate the Bragg peak location can not be applied to the reconstructed profiles. To estimate the PG deduced proton range from the curves in figure 18, we calculate the estimated fall-off as a mean over a range of percentages with the method described in section 2.3.

In order to account for the observed variability, the values for p_{\min} and p_{\max} have to be set individually for each type of profile (namely total, R_1 , R_2 , R_3). For each given profile we define the error function F of variables $(p_{\min}, p_{\max}) \in [0.2, 1]^2$, $p_{\min} \leq p_{\max}$ by the relation:

$$F(p_{\min}, p_{\max}) = |\hat{d}_{p_{\min}, p_{\max}} - d|, \quad (10)$$

where $\hat{d}_{p_{\min}, p_{\max}}$ is the estimated position of the fall-off given by (8) and d is the reference value obtained from simulations. The mean over the three beam energies of the error functions is shown in figure 19 for the four considered PG energy window.

The minimum value of each function F gives the combinations (p_{\min}, p_{\max}) that minimize the error on the estimated PG deduced proton range. However, a best combination is curve-specific. For each PG energy window we dispose of three curves, corresponding to the three beam energies. In what follows we apply a leave-one-out approach to find a best combination (p_{\min}, p_{\max}) and then to calculate the errors on the estimated PG deduced proton ranges shown in table 2. E.g. when the reference values of the fall-off position are considered as known

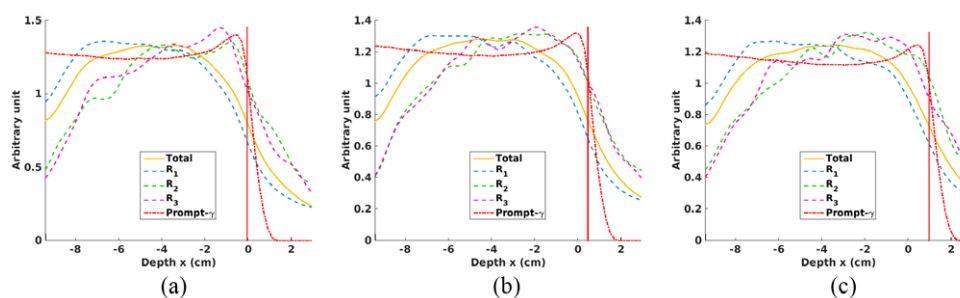


Figure 18. Overlay of the PG profile (dotted red line) and the reconstructed profiles calculated as projection of the central slice on 1 cm around the line $y = 0$ cm. The vertical red line stands for the PG fall-off. (a) [120 MeV] (b) [123 MeV] (c) [126 MeV].

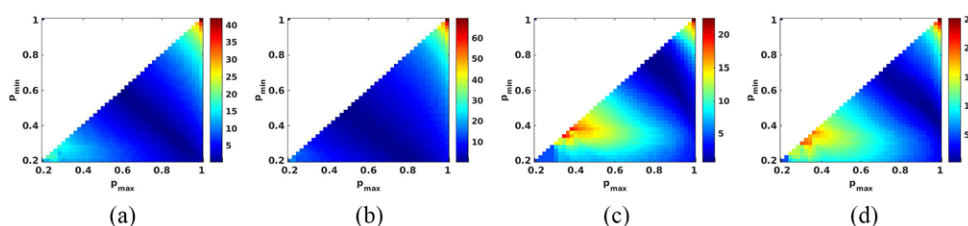


Figure 19. Mean over the three beam energies of the error functions F for four energy windows. (a) Total. (b) R_1 . (c) R_2 . (d) R_3 .

Table 2. Error on the estimated PG deduced proton range, in millimeters.

Beam energy	120 MeV				123 MeV				126 MeV			
PG range (mm)	100				105				110			
Energy window	Total	R_1	R_2	R_3	Total	R_1	R_2	R_3	Total	R_1	R_2	R_3
Error (mm)	0.9	0.6	2.8	1.6	1	0.7	-0.7	1.5	-0.6	-0.6	1.3	0

Note: The error is calculated as the difference $\hat{d}_{p_{\min}, p_{\max}} - d$.

for the beam energies 120 and 123 MeV, for each energy window, two error functions can be calculated. The argument of the minimum of their mean is set as the best combination of percentages. The errors on the estimated position of the fall-off are then calculated for the test energy 126 MeV and are shown in the last four columns of table 2.

The three beam energies we chose, namely 120, 123 and 126 MeV, provide about 5 mm shifts in the position of the Bragg peak. The shifts in the PG profiles observed from the reconstructed images are compared to the theoretical values in table 3. The shifts were calculated for the test samples, i.e. for each beam energy the coordinates of the PG profile fall-off is evaluated with the percentages estimated from the two other energies.

4. Discussions and conclusions

The distribution of the prompt-gamma emission during irradiation in proton therapy is closely related to the deposited dose. The goal of this work was double. On one hand, we investigate the ability of a specific Compton camera and a proposed reconstruction algorithm to provide an image of the distribution of the PG emission with and without energy selection. On the

Table 3. Shifts measured from the reconstructed profiles for different beam energies.

Beam energies increase	120–123 MeV				123–126 MeV			
Reference PG shift (mm)	5				5			
Energy window	Total	R_1	R_2	R_3	Total	R_1	R_2	R_3
Estimated shift (mm)	5.3	5.2	1.6	5	3.5	3.9	7	3.6

other hand, we proposed a method for the estimation of the PG fall-off and we showed that it allows to detect shifts with millimetre accuracy when some prior experience is available.

The spatial distribution of the photons varies with the energy, and some energies were previously shown to characterize the end-of-range of the beam. Imaging of the PG emission for specific energy windows could thus give important information on the treatment. We show that when the initial energy of the photons is known, the reconstructed images relatively well reproduce the simulated distributions up to 5.5 MeV. However, as the PG initial energy can not be sorted, a selection window can be applied only to the total energy deposited by each individual photon. As a consequence, for each selection, the reconstructed image is contaminated with noise caused by incomplete absorption of higher energy photons.

The performances of the Compton camera simulated for this work are better for the window $R_1 = [0.5, 2.5]$ MeV. Compared to other windows, the R_1 window is more advantageous since it benefits from a larger statistics and presents a lower variance. Moreover, the selection on energies below 2.5 MeV leads to an image similar to the one of the total distribution. The available number of events is still in the same order of magnitude. Nevertheless, this energy window is in practice the most affected by noise from neutrons.

The depth of the distal edge of the PG distribution was calculated from the reconstructed images as the coordinate of some percentage of the maximum of the projected profile. For the total distribution, the percentage was previously learned on a set of 100 samples of low-statistics reconstructed images. We observed mild influence of the beam energy on the median percentage. With this approach, we observed less than 1 mm offset between the depths of the fall-off for the reconstructed and simulated profiles. We also evaluated the errors, for four energy windows, when only two samples are available in the learning set. In this case the maximum error we found was of about 3 mm. We also noticed that the smoother the distribution, better the estimation of the fall-off is. With the considered camera, the best values were found for the total and R_1 energy windows. Theoretical shifts of 5 mm in the range of the beam were then estimated with an error lower than 1 mm for the R_1 window. For the higher energy windows the error attained at its maximum 3.4 mm. In the case of a real treatment, the PG profile would present more variability. The machine learning approach proposed in Gueth *et al* (2013) would be then better suited and could be carried on data simulated from the treatment plan.

All the typical noise sources in PG imaging were not taken into account in this work. The attenuation in the emitting volume was not discussed here because in the described context it had no significant influence on the reconstructed images. Random coincidences were also avoided in our simulations by recording the interactions of each particle separately. The noise coming from neutrons was ignored here, but it was quantified as very important at low energies in other works. Consequently, the Compton camera would also detect neutrons in the energy window R_1 and the results we obtained for this window are likely to be affected. Exploitation of high energy photons may be a solution but requires an enhancement of the detection efficiency compared to our set-up. In clinical practice, importance should be accorded to the ability of a detector to accurately measure the initial energy of the photons.

Discrepancies with the treatment plan also arise from volume composition changes due to misplacements of the patient, anatomical evolution or wrong estimation of the stopping power

of the tissues. Since the emission spectrum is tissue dependent, the precise estimation of the joint spatial and energy distribution is an important issue in protontherapy monitoring.

Acknowledgment

This work was partly supported by the ENVISION project (co-funded by the European commission under the FP7 Collaborative Projects Grant Agreement Nr. 241851FP7), by ETOILE's Research Program (PRRH/UCBL, under CPER 2007-13 funding) and by the LABEX PRIMES (ANR-11-LABX-0063) of Université de Lyon. The authors would like to thank the anonymous reviewers for careful reading of the manuscript and thoughtful comments.

References

- Bom V, Joulaeizadeh L and Beekman F 2012 Real-time prompt gamma monitoring in spot-scanning proton therapy using imaging through a knife-edge-shaped slit *Phys. Med. Biol.* **57** 297
- Cambráia Lopes P C, Pinto M, Simões H, Biegun A, Dendooven P, Oxley D, Parodi K, Schaart D and Crespo P 2012 Optimization of collimator designs for real-time proton range verification by measuring prompt gamma rays *IEEE Nuclear Science Symp. and Medical Imaging Conf.* pp 3864–70
- Compton A H 1923 A quantum theory of the scattering of x-rays by light elements *Phys. Rev.* **21** 483
- Frandes M, Zoglauer A, Maxim V and Prost R 2010 A tracking Compton-scattering imaging system for hadrontherapy monitoring *IEEE Trans. Nucl. Sci.* **57** 144–50
- Gillam J E, Lacasta C, Torres-Espallardo I, Juan C C, Llosá G, Solevi P, Barrio J and Rafecas M 2011 A Compton imaging algorithm for on-line monitoring in hadrontherapy *SPIE Medical Imaging 2011: Physics of Medical Imaging Conf.* vol 7961
- Golnik C *et al* 2014 Range assessment in particle therapy based on prompt γ -ray timing measurements *Phys. Med. Biol.* **59** 5399
- Gueth P, Dauvergne D, Freud N, Létang J, Ray C, Testa E and Sarrut D 2013 Machine learning-based patient specific prompt-gamma dose monitoring in proton therapy *Phys. Med. Biol.* **58** 4563
- Janssen F, Landry G, Lopes P C, Dedes G, Smeets J, Schaart D, Parodi K and Verhaegen F 2014 Factors influencing the accuracy of beam range estimation in proton therapy using prompt gamma emission *Phys. Med. Biol.* **59** 4427–41
- Jan S *et al* 2011 GATE V6: a major enhancement of the GATE simulation platform enabling modelling of CT and radiotherapy *Phys. Med. Biol.* **56** 811–901
- Kanawati W E, Létang J, Dauvergne D, Pinto M, Sarrut D, Testa E and Freud N 2015 Monte Carlo simulation of prompt γ -ray emission in proton therapy using a specific track length estimator *Phys. Med. Biol.* **60** 8067–86
- Kim D, Yim H and Kim J W 2009 Pinhole camera measurements of prompt γ -rays for detection of beam range variation in proton therapy *J. Korean Phys. Soc.* **55** 1673–6
- Kormoll T, Fiedler F, Schöne S, Wüstemann J, Zuber K and Enghardt W 2011 A Compton imager for *in vivo* dosimetry of proton beams—a design study *Nucl. Instrum. Methods Phys. Res. A* **626** 114–9
- Krimmer J *et al* 2014 Development of a Compton camera for medical applications based on silicon strip and scintillation detectors *Nucl. Instrum. Methods Phys. Res. A* **787** 98–101
- Kurosawa S *et al* 2012 Prompt gamma detection for range verification in proton therapy *Curr. Appl. Phys.* **12** 364–8
- Lee H R *et al* 2012 Design optimization of a 2D prompt-gamma measurement system for proton dose verification *J. Korean Phys. Soc.* **61** 239–42
- Lojacono X, Richard M H, Ley J L, Testa E, Ray C, Freud N, Létang J M, Dauvergne D, Maxim V and Prost R 2013 Low statistics reconstruction of the Compton camera point spread function in 3D prompt- γ imaging of ion beam therapy *IEEE Trans. Nucl. Sci.* **60** 3355–63
- Mackin D, Peterson S, Bedar S and Polf J 2012 Evaluation of a stochastic reconstruction algorithm for use in Compton camera imaging and beam range verification from secondary gamma emission during proton therapy *Phys. Med. Biol.* **57** 3537–53
- Maxim V, Lojacono X, Hilaire E, Krimmer J, Testa E, Dauvergne D, Magnin I and Prost R 2016 Probabilistic models and numerical calculation of system matrix and sensitivity in list-mode MLEM 3D reconstruction of Compton camera images *Phys. Med. Biol.* **61** 243–64

- Maxim V 2014 Filtered backprojection reconstruction and redundancy in Compton camera imaging *IEEE Trans. Image Process.* **23** 332–41
- Min C H, Kim C H, Youn M Y and Kim J W 2006 Prompt gamma measurements for locating the dose falloff region in the proton therapy *Appl. Phys. Lett.* **89** 183517
- Moteabbed M, España S and Paganetti H 2011 Monte Carlo patient study on the comparison of prompt gamma and PET imaging for range verification in proton therapy *Phys. Med. Biol.* **56** 1063–1082
- Ordonez C E, Bolozdynya A and Chang W 1997 Dependence of angular uncertainties on the energy resolution of Compton cameras *IEEE Nuclear Science Symp.* vol 2
- Ortega P G et al 2015 Noise evaluation of Compton camera imaging for proton therapy *Phys. Med. Biol.* **60** 1845–63
- Perali I et al 2014 Prompt gamma imaging of proton pencil beams at clinical dose rate *Phys. Med. Biol.* **59** 5849–71
- Pinto M, Dauvergne D, Freud N, Krimmer J, Létang J M, Ray C, Roellinghoff F and Testa E 2014 Design optimization of a TOF-based collimated camera prototype for online hadrontherapy monitoring *Phys. Med. Biol.* **59** 7653–74
- Polf J, Panthi R, Mackin D, McCleskey M, Saastamoinen A, Roeder B and Beddar S 2013 Measurement of characteristic prompt gamma rays emitted from oxygen and carbon in tissue-equivalent samples during proton beam irradiation *Phys. Med. Biol.* **58** 5821–31
- Polf J, Peterson S, Ciangaru G, Gillin M and Beddar S 2009 Prompt gamma-ray emission from biological tissues during proton irradiation: a preliminary study *Phys. Med. Biol.* **54** 731–43
- Richard M H et al 2012 Design study of the absorber detector of a Compton camera for online control in ion beam therapy *IEEE Trans. Nucl. Sci.* **59** 3496–500
- Roemer K et al 2015 Characterization of scintillator crystals for usage as prompt gamma monitors in particle therapy *J. Instrum.* **10** P10033
- Sarrut D et al 2014 A review of the use and potential of the GATE Monte Carlo simulation code for radiation therapy and dosimetry applications *Med. Phys.* **41** 064301
- Shepp L A and Vardi Y 1982 Maximum likelihood reconstruction for emission tomography *IEEE Trans. Med. Imaging* **1** 113–22
- Smeets J et al 2012 Prompt gamma imaging with a slit camera for real-time range control in proton therapy *Phys. Med. Biol.* **57** 3371
- Smith B 2005 Reconstruction methods and completeness conditions for two Compton data models *J. Opt. Soc. Am. A* **22** 445–59
- Stichelbaut F and Jongen Y 2003 Verification of the proton beam position in the patient by the detection of prompt gamma-rays emission *39th PTCOG Meeting (San Francisco)*
- Styczynski J, Riley K, Binns P, Bortfeld T and Paganetti H 2009 Su-dd-a3-03: can prompt gamma emission during proton therapy provide *in situ* range verification? *Med. Phys.* **36** 2425
- Testa E, Bajard M, Chevallier M, Dauvergne D, Foulher F L, Freud N, Létang J M, Poizat J, Ray C and Testa M 2009 Dose profile monitoring with carbon ions by means of prompt-gamma measurements *Nucl. Instrum. Methods Phys. Res. B* **267** 993–6
- Tomitani T and Hirasawa M 2002 Image reconstruction from limited angle Compton camera data *Phys. Med. Biol.* **47** 2129–45
- Verburg J M, Riley K, Bortfeld T and Seco J 2013 Energy- and time-resolved detection of prompt gamma-rays for proton range verification *Phys. Med. Biol.* **58** L37–49
- Verburg J M and Seco J 2014 Proton range verification through prompt gamma-ray spectroscopy *Phys. Med. Biol.* **59** 7089
- Wilderman S, Fessler J, Clinthorne N, LeBlanc J and Rogers W 2001 Improved modeling of system response in list mode EM reconstruction of Compton scatter camera images *IEEE Trans. Nucl. Sci.* **48** 111–6
- Wilderman S J, Clinthorne N H, Fessler J A and Rogers W L 1998 List-mode maximum likelihood reconstruction of Compton scatter camera images in nuclear medicine *IEEE Nuclear Science Symp. Conf. Record* vol 3 pp 1716–20
- Zhang B and Zeng G L 2007 Two-dimensional iterative region-of-interest (ROI) reconstruction from truncated projection data *Med. Phys.* **34** 935–44
- Zoglauer A, Andritschke R and Schopper F 2006 MEGALib—the medium energy gamma-ray astronomy library *New Astron. Rev.* **50** 629–32
- Zoglauer A, Weidenspointner G, Galloway M, Boggs S and Wunderer C 2009 Cosima—the cosmic simulator of MEGALib *Nuclear Science Symp. Conf. Record* pp 2053–9